

Bi growth on Al-Pd-Mn Quasicrystal

Abstract

Spectroscopic techniques are employed to examine Bismuth (Bi) growth on icosohedral Aluminium-Palladium-Manganese Quasicrystal (i-Al-Pd-Mn). The study complements previous work on the same system examined with Scanning probe microscopy¹². The time take, t , to deposit a monolayer of Bi at 120nA Bi flux was $t = 31 \pm 3$ minutes, in good agreement (within one standard deviation) with 33.3 minutes as calculated by Smerdon et al¹. X-ray Photoelectric Spectroscopy (XPS) is used to determine elemental composition of the sample through the temperature range 300 – 525 degrees. The Bi multilayer desorbs between 275 and 300 degrees. The Bi monolayer desorbs at approximately 500 degrees. Results on the inelastic mean free path (IMFP) of electrons through Bi indicate a large discrepancy between the theoretical predictions and the measured value.

Introduction

The discovery of a three-dimensional state with short-range translational order but only bond orientational long range order³ followed the demonstration of atomic scale topographic images from scanning tunnelling microscopy⁴ (STM). These so called *Quasicrystals* are non-crystalline materials with perfect long-range order, but with no three-dimensional periodicity⁵. The unique properties of Quasicrystals, low friction⁶ and negative gradients on resistance-temperature plots⁷, has driven some research towards single element Quasicrystalline growth⁸.

Franke et als' careful comparison of clean Al-Pd-Mn and Bi monolayer Al-Pd-Mn LEED patterns revealed quasicrystalline bismuth growth in 2002⁹. This work motivated a first principles study of Quasiperiodic Bi monolayer on Al-Pd-Mn to map the high-energy landscape of the surface indicating the most stable positions of adsorbed atoms¹⁰. These *ab initio* results were not observed at the University of Liverpool where Bi atoms where found to nucleate on truncated pseudo-Mackay clusters^{1, 11}. Further research indicates that Bi on Al-Pd-Mn has a low sticking coefficient and that, beyond the wetting layer, Bi islands grow with heights of 4 atomic layers or integer multiples of this height².

This project will investigate and extend previous research into Bi on Al-Pd-Mn using predominately spectroscopic apparatus under Ultra high vacuum (UHV) $\sim 10^{-10}$ mbar.

Theory/Equipment

Attaining and maintaining UHV for the entirety of the experiment is achieved with various pieces of apparatus. The vacuum chamber and associated pipework are made of stainless steel, which does not corrode or rust and has a low rate of outgassing of adsorbed gas. The vacuum joints are made with flat copper gaskets. A roughening pump was used at room temperature to reduce the pressure inside the chamber to the millibar (mb) range. Once the roughening pumps achieved a pressure of 10^{-4} mb the ion pump was engaged. The ion pump consists of a cathode and a tube shaped anode under a high potential difference (P.d.). The large voltage strips electrons from the molecules present in the system. Ions, created in this process, are accelerated to the negative cathode. The magnetic field, induced by the tube shaped anode, forces the liberated electrons to follow a helical path. This increases the path length of the electron, increasing the chance of collision with gas molecules, repeating the process. The ions and electrons produced are adsorbed by the cathode and anode respectively, reducing the pressure in the chamber¹². The vacuum chamber was heated to 470 Kelvin while vacuum pumps operate. Baking the chamber accelerates desorption of water vapour and other gases from internal surfaces. When cooled to room temperature the pressure inside the chamber dropped to the 10^{-10} mb range. An ionization gauge monitored the pressure inside the chamber. Thermally emitted electrons from the ionization gauges' cathode are accelerated by the anode potential, which ionise gas molecules in their path. The ion current measured by the collector is related to the ambient pressure¹².

Although the sample was mounted in the chamber prior to bake out, the constraints', imposed by the structure of the chamber, demand that the sample be manipulated while inside the chamber at UHV (*in situ*). The sample was transported between the chambers by magnetically-coupled specimen transfer loaders. Magnetic coupling is used in place of sliding o-ring seals to maintain better vacuum levels.

Without an adequate cleaving method for Quasicrystals the sample must be cleaned in the chamber under UHV to ensure experimental results are not originating from surface contaminants. Impurities in the top most layers of the i-Al-Pd-Mn were removed via bombardment with Argon (Ar) gas ions, a 50 year old process¹³ referred to as *sputtering*. The ion bombardment yields a pitted and rough surface. By heating the sample to just below its melting temperature desorption of impurities and bulk defects is accelerated, yielding a smoother clean surface. A strict procedure is laid out for the sputtering of the sample. Upon switching on the ion pump valve the ion energy is increased to 2.54kV. The current on the filament is increased slowly up to 2.49 mA to avoid destroying the element. The tap separating the exit of the Ar canister and the chamber is slowly opened producing a flux of Ar into the chamber. The tap is opened until the pressure inside the chamber increases to 10^{-7} mb. At this pressure the amp meter displays a nanoamp reading with 10microamps most desirable.

X-ray photoelectron spectroscopy was the principle technique used to analyse the Bi i-Al-Pd-Mn system. This technique is based on Einstein's photoelectric effect¹⁴, where photons can induce electron

emission from a solid if the photon energy $h\nu$ is greater than the work function of the solid ϕ . The kinetic energy of the emitted electrons E_{kin} is given by the photoelectric equation.

$$E_{Kin} = h\nu - E_B - \phi \quad 1$$

E_B is the binding energy of electron in the solid, measured with respect to the Fermi level. The binding energy is determined by measuring the kinetic energy of the liberated electrons. Electrons liberated below the surface are unlikely to avoid collisions and so rarely leave the solid with their original energy. The peaks described by equation 1, therefore, are predominately expressing information from the surface. If it is assumed that only inelastic scattering is responsible for electron attenuation then the Beer-Lambert law¹⁵ can be invoked.

$$I_z = I_0 \cdot e^{(-z/\lambda \cdot \cos\theta)} \quad 2$$

Where I_z is the intensity emanating from the atoms at depth z , I_0 is the intensity from the surface atoms, θ is the electron take off angle with respect to the surface normal and λ the electron inelastic mean free path (IMFP). For the sample consisting of an overlayer of Bi on a substrate of inhomogeneous material the Beer-Lambert Law can be written as

$$\ln(I_m) - \ln(I_c) = \frac{-z}{\lambda \cdot \cos(\theta)} \quad 3$$

Where I_m is the Intensity of the selected peak with a monolayer of Bi on the sample and I_0 is the intensity of the selected peak with a clean sample. A plot of $\ln(I_m) - \ln(I_c)$ as a function of $1/\cos(\theta)$ will produce a gradient of $\frac{-z}{\lambda}$.

The X-rays are produced by bombardment of a metallic target with high-energy electrons. The high energy electrons are produced by a “dual anode” device¹⁶ first tested in 1973¹⁷. This device incorporates magnesium (Mg) and Aluminium (Al) coated anodes, with separate filaments to excite the respective faces. The anode was operated with a voltage of 10 Kilo Volts (kV) such that electrons are ripped from

the earthed filament and accelerated to the anode. Accelerated electrons collide with and release anode bulk electrons from tightly bound inner electron shells. Electrons from higher, less tightly bound, levels fill the vacancies and the surplus energy is then transferred to the emission of an X-ray photon¹⁸. The Al K α anode was used in this experiment producing X-rays with characteristic energy of 1486.6 electron volts (eV) and a full width half maximum (FWHM) of approximately 0.85 eV¹⁹. The K α line is an unresolved doublet (K α_1, α_2), arising from the transitions 2p_{3/2} to 1s, or 2p_{1/2} to 1s in the ionised target atoms. The large amounts of heat generated in this process are controlled by water cooling the anode. In depth analysis¹⁷ has shown that some electrons produce photons with a range in energy due to their coulomb induced deceleration (bremsstrahlung radiation).

A step by step procedure was received for the operation of the X-rays. The first instruction is to switch on the water for the X-rays so that none of the apparatus overheats. The voltage is increased until a few kV is attained, then the filament current is slowly increased to 2.56 Amps. The voltage is then increased to a value of 10.02 kV or until the emission current reads 9.6mA theoretical. Finally the multiplier is increased to 2.1

Without proof, the photoelectron intensity per X-ray photon of energy $h\nu$ is obtained from earlier work^{20, 21}

$$I_i = I_0 \eta_i \sigma_i \lambda_T(\varepsilon_i) D(\varepsilon_i) \quad 4$$

Where I_0 is the X-ray flux; η_i is the density of atoms of type i ; σ_i is the photo-excitation probability; $\lambda_T(\varepsilon_i)$ is the mean free path of photoelectron with energy ε_i , in the specimen and $D(\varepsilon_i)$ is the fraction of electrons detected by the analyser/detector combination¹⁹.

The next step in the information chain of the XPS instrument is the analyser. Although magnetic analysers were used in the infancy of spectroscopic experiments²², the analyser used in this project exploits the field of electrostatics. Much of the early developments²³ in the electrostatic hemispherical analyser (HSA), used in this experiment, arrived long before the advent of UHV capabilities²⁴. As the name suggest the HSA consists of two electrically isolated concentric hemispheres in conjunction with an electro-static electron-lens system. A potential difference between the inner and outer hemispheres is applied which separates electrons by allowing only electrons of a chosen kinetic energy (the pass energy (CPA)) through to the detector.

Apparatus to detect the energy analysed electrons is situated at the exit of the HSA. The number of electrons contributing to the analysis is increased by a channel electron multiplier (CEM). The CEM consists of small diameter semiconducting glass tube with approximately 2 – 4 volts applied along its length. Secondary electrons are produced when incident electrons collide with the wall of the CEM²⁵. A cascade of electrons is produced after several cycles of electron-wall collisions. The CEM used was

curved to prevent ionic feedback and to optimise the number of collisions. The CEM has a diameter of tens of μm so hundreds of thousands of CEMs can be placed in parallel in a channel plate¹⁹. Under optimal conditions the CEM achieves gains greater than 10^4 .

The main experiment involves the liberation of sample electrons by incident X-ray photons while under UHV (*in vacuo*). The sample electrons are accelerated by the electric field of the X-ray photon and secondary X-rays, with the same wavelength and phase as the incident radiation, are emitted. The number of electrons in the atom determines the amplitude of the diffracted X-rays and is highly dependent on the diffraction angle⁵. The X-rays penetrate many micrometres into the bulk however the photo-electrons can only travel a few atomic layers²⁶, delivering high surface sensitivity. The photoelectron emission is energy analysed to produce a spectrum of electron intensity as a function of energy: the X-ray photoelectron spectrum.

Other techniques used in this project include low energy electron diffraction (LEED). The diffraction pattern observed when an electron beam irradiates a sample is found by construction of the Ewald Sphere. The physical basis for diffraction experiments lies in the interference effects produced by phase differences between rays elastically scattered from different atoms in the crystal. A collimated beam of monochromatic rays with a wavevector k irradiates the sample. Two adjacent atoms x and y , will scatter the rays such that a phase difference Δ arises due to their separation.

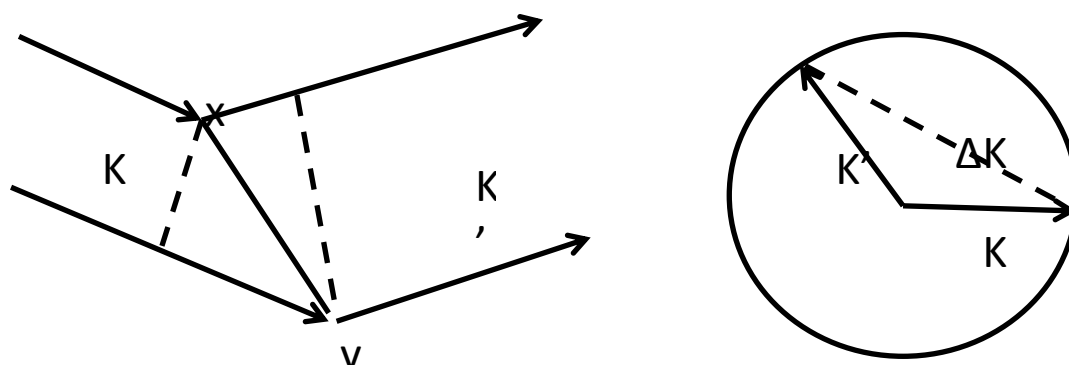


Figure 1 An incoming plane wave k is scattered by two atoms. Figure 2. A sphere of radius $2\pi/\lambda$ is drawn in reciprocal space with the vector k appropriately oriented.

The Ewald sphere has a

radius of $2\pi/\lambda$ in reciprocal space so that the permitted diffracted waves are then determined by the reciprocal lattice points lying on this sphere. A thorough analysis of atomic form factors and reciprocal space momentum vectors⁵ leads to Bragg's Law for constructive interference.

$$2a \cdot \sin \theta = \lambda$$

5

Where a is the lattice spacing and θ is the angle of beam incidence (zero for LEED). The wavelength is typically short compared to the radius ($1/\lambda$) of the Ewald sphere. To a good approximation the Ewald sphere is plane where the diffraction pattern is formed. For quasicrystalline samples, points in reciprocal space are broadened and look rather like small line segments due to the thickness of the sample. Icosahedrons have six 5-fold axes, ten 3 fold axes and fifteen 2-fold axes. Much work has been published on the indexing of different directions^{27,28} however this is beyond the scope of this project which will use LEED patterns to complement other sources of data.

STM data has also been taken to increase the understanding of the system being studied. STM relies on an explicit manifestation of quantum mechanics, termed quantum mechanical tunnelling²⁹⁻³¹. Contrary to classical mechanics the particle penetrates through a potential barrier higher than its kinetic energy. It is this tunnelling affect which allows electrons from a tip to travel through a vacuum environment such that a current is achieved. The apparatus for STM at the University of Liverpool Chadwick laboratory consists of an atomically sharp tip mounted upon a set of piezoelectric transducers supported very close to the sample surface. The tip is engineered to have an atomically sharp tip by using a short duration voltage pulse (5-10V) such that atoms are field emitted from the tip¹². The application of a potential difference induces a tunnelling current with exponential dependence of the separation of tip and sample. If the surface is positive with respect to the tip then electrons tunnel out of the tip (*vice versa* for negative). The density of occupied electronic states in the conduction band of the tip contributes to the current. Further, the electrons can only tunnel if there are empty states in the electronic structure of the surface. The current depends upon the density of occupied states in the tip, the density of unoccupied states in the surface and the probability of crossing the intervening vacuum gap by tunnelling. The apparatus is isolated from vibration by mounting the tip-sample assembly on a critically damped anti-vibration suspension.²⁸

Results / Measurements

Work in the Chadwick laboratory was orchestrated by Kirsty Young under the guidance of Dr. V. Dhanak. With no formal training on how to use a large array of expensive equipment, my approach involved trying to learn quickly but not to hinder the work of physicists with superior and necessary experience on the equipment. With the sample *in situ*, the apparatus was prepared for the first XPS spectrum. Three manipulators enable the sample to be moved in all three space directions. The vertical manipulator has an extra degree of freedom, which enables the sample to be rotated around the vertical

axis. Through discussion with the previous experimenter³², and direct observation of the sample in the chamber a set of four co-ordinates (Euclidian and one angular) for the XPS experiment was recorded.

The first XPS spectrum reveals the peaks; Pd3d, Al2s, Al2p, oxygen 1s (O1s), OKLL and a carbon 1s (C1s) peak, with reference to previously identified peaks³³. The free bonds at the surface of the Quasicrystal sample will have been saturated by oxygen present in the atmosphere prior to the experiment. It is not uncommon to observe carbon peaks in an un-cleaned sample when it has previously been cleaned by diamond paste. After sputtering and annealing the sample the Mn2p peak

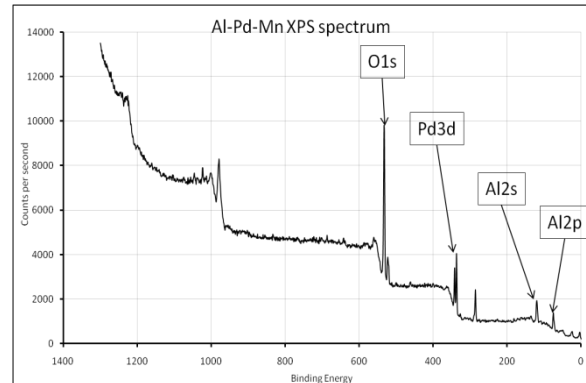


Figure 3. XPS spectrum of uncleaned sample in situ

is revealed and the oxygen and carbon peaks have disappeared. The quantitative nature of XPS allows for elemental analysis of the clean sample. The intensity of a peak is directly proportional to the density of the atom from which it derives within the sampled volume¹⁹. The relative atomic concentration of any chosen element, A, is obtained from

$$C_A = \frac{I_A/S_A}{\sum_n \frac{I_n}{S_n}} \quad 5$$

Where C_A is usually expressed as atomic %. The n elements give measured intensities of I_A to I_N and the peaks are associated with relative sensitivity factors S_A to S_N . As the sample is not homogeneous this formula is only used to provide an estimate of the atomic constituents of the Al-Pd-Mn sample.

Element	Percentage	δ
Al	78.1%	3.9%
Pd	16.4%	0.8%
Mn	5.5%	0.3%

Table 1. Atomic constituents of the i-AlPdMn sample

As the XPS is surface sensitive and the sample is cut to reveal aluminium rich surface, this estimation will be exaggerated in aluminium.

Previous research into Bi evaporated onto Al-Pd-Mn Quasicrystal revealed a deposition rate of approximately 1.8 Monolayer (ML) per hour, at a Bi flux of 120nA^1 . At this flux 1 ML should be deposited at approximately 33 minutes. Other research also indicates that upon completion of a

monolayer the bismuth continues growing with island formation atop the wetting layer². These islands are observed to have magic height of four atomic layers² i.e. the height of the islands are integer multiples of four atomic heights. This so called Strankski-Krastanov³⁴ growth can be verified by plotting the XPS line intensity of the overlayer as a function of time. The plot produced should have one inflexion point if the growth mode is layer then island³⁵⁻³⁸. The break in the gradient arises due to the overlayer covering a relatively small part of the monolayer when growing in island formation so that the X-rays still penetrate the substrate at high coverage. The gradient after the breakpoint is then dependent on the island density and shape. Stranksi-Krastanov arises when a lattice mismatch between the substrate and the film does not continue beyond a certain film thickness.

Initially Bi was evaporated at a flux of 120nA in accordance with work by Smerdon et al¹. The deposition ran for 20 minutes and no break was observed in the gradient of the bismuth peak intensity. It was felt³⁹ that the experiment would take too long at 120nA Bi flux and so the flux was increased to 400nA and the deposition started again on a clean surface. At this rate of flux a break in the gradient on the intensity-time plot is clearly observed. The raw data measured from the apparatus was the peak intensity i.e. the height of the peak and the time of deposition. The software package Casa XPS⁴⁰ was used to ascertain the height of the peak with the background radiation removed. Each elemental peak has an intrinsic sensitivity factor associated with Atomic number and interaction cross section. The relevant experimental sensitivity factors³³ were used to normalize the peak intensities. The data is presented in a plot of Elemental percentage as a function of deposition time, using equation (page 6) to determine the elemental percentage. The software package Java JLinefit⁴¹, which uses the suitably weighted squared difference between a set of measurements and their predicted values, was used to create a straight line fit to the data. The error on the intensity was estimated to be the height of the noise on the background of the spectrum. The error on the sample element percentages were deduced from adding the fractional errors in quadrature.

The break in the gradient is clearly observed in figure 5. The two straight lines in figures 5 and 6 were solved such that the intersection would indicate the time in minutes taken to deposit a monolayer. The data presented in figure 5 produced a point of inflexion at 7.9 ± 5.9 minutes. The data presented in figure 6 produced a point of inflexion at 7.8 ± 3.5 minutes. The large errors in the values arising from the large amounts of noise in the background of the spectra used to determine the intensities. With two sets of deposition data for Bi flux of 120nA and 400nA, it is interesting to consider whether the relationship between the flux and the deposition is linear. Figures 8 and 9 indicate that at 400nA Bi flux more bismuth is being deposited than the ratio 400/120, although the difference is within the margin of error. The constraints of experimental time did not allow a thorough investigation into the relationship between deposition and flux, however; the relationship is considered to be not far from linear. With this in mind, experimental peak intensities for 120nA and 400nA flux were combined and

normalised to a flux of 120nA to check for agreement on the deposition of a monolayer with Smerdon et al.

Figures 10, 11, and 12 display data taken with the sample at an angle of 15° to the analyser. Figures 13, 14, and 15 display data taken with the sample at an angle of 75° to the analyser. At the grazing angle the sample percentage of Bi is higher due to more of the analysed electrons arriving from the topmost layers of the sample. Four values of the inflexion point are extrapolated from the two sets of angles and two sets of peaks analysed. The four values are averaged to give an inflexion point of 31 minutes the error is taken to be the standard deviation or standard error on the mean

$$\Delta t = \sqrt{\frac{\sum(t_i - \bar{t})^2}{N(N-1)}} \quad 6$$

Where t is the time taken to deposit a monolayer of bismuth onto the sample and N is the number of values of t . The value of t is calculated as $t = 31 \pm 3$ minutes in good agreement (within one standard deviation) with 33.3 minutes as calculated by Smerdon et al¹.

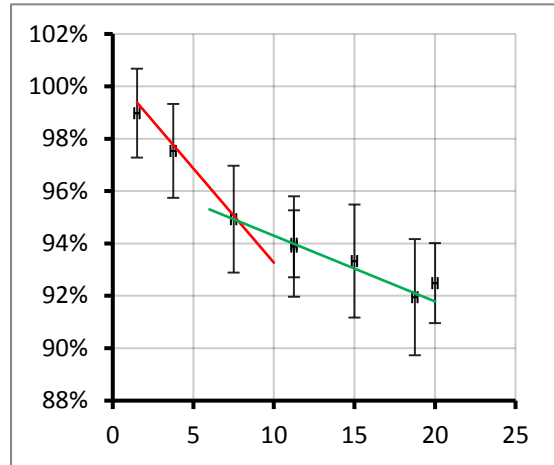
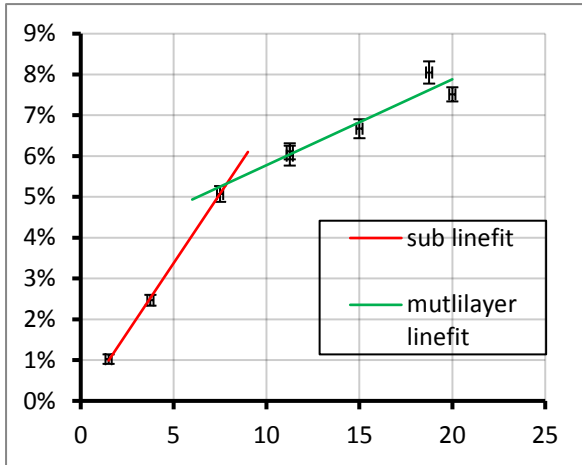


Figure 5. Bi sample percentage as a function of time at 400nA Bi flux. Figure 6. AIPdMn sample percentage as a function of time at 400nA Bi flux

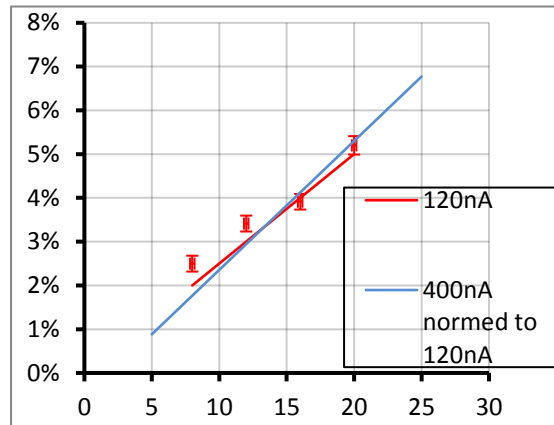
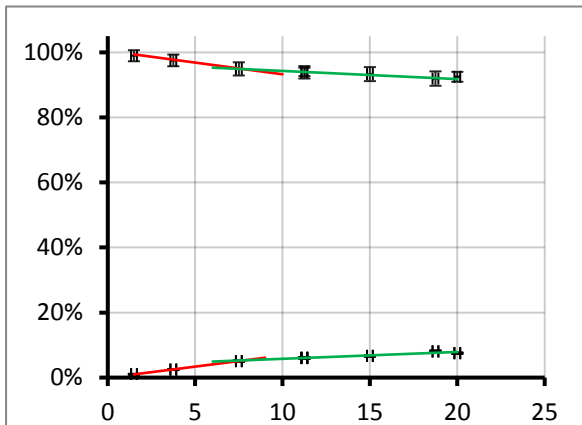


Figure 7. AIPdMn and Bi sample percentage as a function of time at 400nA Bi flux. Figure 8. Bi sample percentage as a function of time at 120nA Bi flux with 400nA Bi flux normalized to 120nA superimposed.

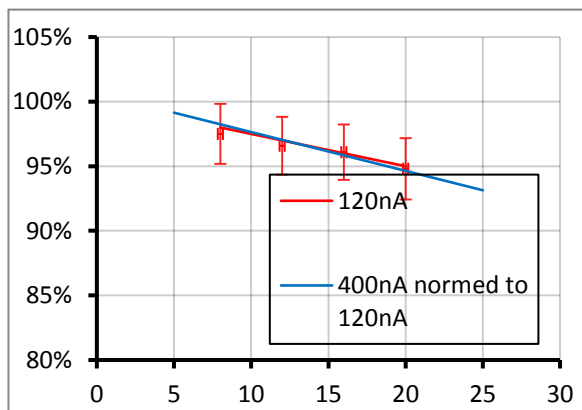


Figure 9. AIPdMn sample percentage as a function of time at 120nA Bi flux with 400nA Bi flux normalized to 120nA superimposed

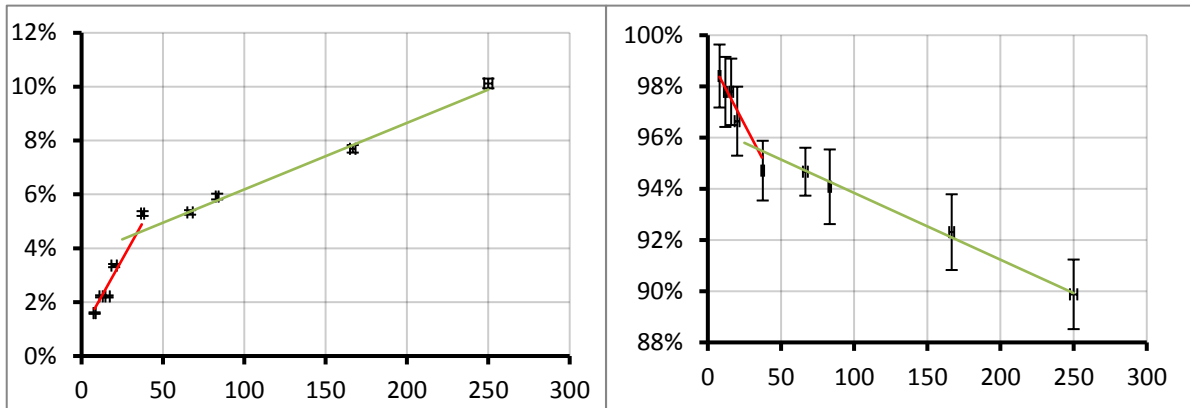


Figure 10. Bi sample percentage as a function of deposition time at 120nA Bi flux. Figure 11. AIPdMn sample percentage as a function of deposition time at 120nA Bi flux

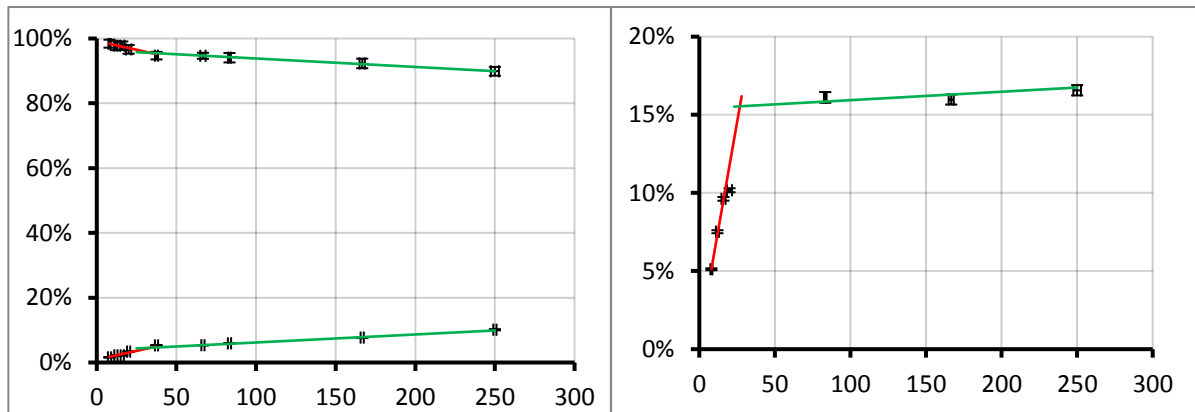


Figure 12. AIPdMn sample percentage as a function of deposition time at 120nA Bi flux. Figure 13. Bi sample percentage as a function of deposition time at 120nA Bi flux with the sample at a grazing angle to the analyser

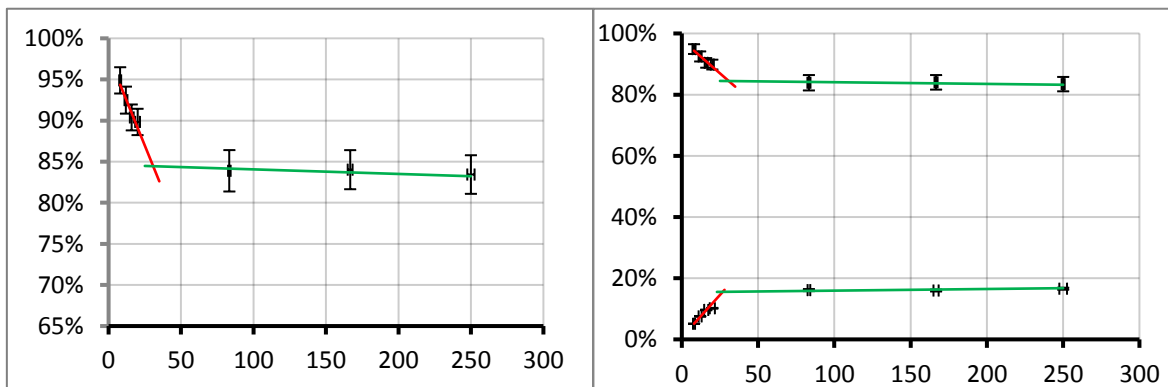


Figure 14. AIPdMn sample percentage as a function of deposition time at 120nA Bi flux with the sample at a grazing angle to the analyser. Figure 15. Bi and AIPdMn sample percentage as a function of deposition time at 120nA Bi flux

The experimental set up at this stage was discussed and it was concluded that co-ordinates for the bismuth deposition had not been satisfactorily arrived at. The Bismuth evaporator produced a beam of Bi in the vacuum chamber and the aim was to direct the beam onto the centre of the sample. An innovative step taken at this stage was to turn off all the lights in the laboratory and to observe the reflection of the Bi beam on the sample. Although rudimentary, this technique indicated that the Bi beam was in the right vicinity, although it appeared as though the beam was too narrow to cover the whole of the sample. The XPS software "Spectra 8" was manipulated so that the live number of counts per second for a particular peak was displayed. The position of the sample was then changed while the counts per second were monitored. The sample was placed in the position that produced the highest counts per second. The area of the aperture leading to the hemispherical analyser was then changed as the counts per second were recorded. Had the Bi beam not covered the entire sample, decreasing the area of the aperture would have led to an increase in the Bi peak relative to the sample peak. No such increase was observed.

The work of Sharma et al² indicated that Bi islands will desorb from the surface of Al-Pd-Mn Quasicrystal at 523 Kelvin. To investigate this further the project looked at the bismuth desorption (*top down*) from the sample at various temperatures. Initially 1000nA flux of Bi was deposited for 25 minutes to ensure Bi was deposited beyond the monolayer and into the multilayer. The sample holder has an electric sample heater controlled by varying the current through the heating filaments. The current was increased through the range 0.5 amps to 5.5 amps for ten minute intervals and the peak intensities recorded. The peak intensities were used to calculate the sample constituent percentages using equation 5. The common consensus was that the bismuth desorption was temperature dependent but not time dependent. To investigate this hypothesis some values of current were recorded for longer than ten minutes, and no significant extra desorption was observed. The extra data on some values of current allowed an average sample constituent to be calculated with a reduced error arising from the standard deviation. The error on the intensities was estimated to be 5% of the intensity as this was consistently close to the value of the background noise. The error on the current was estimated to be plus or minus 25% of the smallest unit, slightly larger than the factory recommended 10% due to the small fluctuation in current on the display. Figure 15 shows the Bi sample percentage as a function of heating element current.

The heating element current was calibrated by plotting the current as a function of temperature, using a pyrometer to record the temperature of the sample. A pyrometer intercepts and measures the thermal radiation from the surface of a sample. Figure 16 shows the relationship between the current and temperature is roughly linear, however; the straight line fit yields a zero current temperature of -30 degrees. The zero current temperature should be approximately room temperature so it was argued that the two lowest current readings were producing a lower temperature reading due to the pyrometer being at the limit of its measurement range. Further the sample was only heated for ten minutes before

the temperature was recorded which may have not allowed adequate time for the sample to reach thermal equilibrium. To satisfy our investigation the temperature calibration was carried out after annealing the sample to 500 degrees, so that the sample temperature would not still be increasing upon measurement. Figure 17 shows the discrepancy between the heated sample and the cooled sample, particularly between the lowest current points. A zero current point of 20 degrees temperature was added to the data to produce figure 18. The straight line of figure 18 was used to plot temperature along the x axis of figures 19 and 20.

Figure 19 indicates that up to a temperature of 275 degrees very little of the bismuth evaporates from the surface. Between 275 and 400 degrees there is a sharp decrease in the percentage of Bi present, interpreted as desorption of the multilayer. A difference in bonding strength between higher layers and layers close to the monolayer could account for the range in temperatures over which the multilayer desorbs. The plateau observed in figure 19 between 400 and 500 degrees suggests that the entire multilayer has been removed and that the monolayer requires greater energy to break the bonds attaching it to the surface. Above 525 degrees the monolayer begins to evaporate although there is still Bi present on the surface at the anneal temperature. Figure 20 is essentially the reverse of figure 19 i.e. the Al-Pd-Mn sample percentage as a function of sample temperature.

The relationship between peak intensities for clean Al-Pd-Mn and monolayer Al-Pd-Mn (equation 3) was used to determine the IMFP of Bi. Previous work on the desorption of Bi demonstrated that the Bi multilayer is desorbed from Al-Pd-Mn at a temperature of 525 degrees. Accordingly the sample was deposited with a large amount of Bi and heated to 525 degrees to obtain a monolayer of Bi on the Al-Pd-Mn sample. The intensities of the various elemental peaks were then measured as the sample-normal to analyser angle was rotated through ten degree intervals from 15 degrees to 75 degrees. The peak intensities were recorded again for the same angles with clean Al-Pd-Mn. The data collected enabled the natural logarithm of the clean minus the monolayer intensity to be plotted as a function of $\frac{1}{\cos\theta}$. The plots should produce a straight with gradient $\frac{d}{\lambda}$, where d has previously been calculated as 1.5Angstroms^{2,12}. The results of the experimental data are summarised in table 2

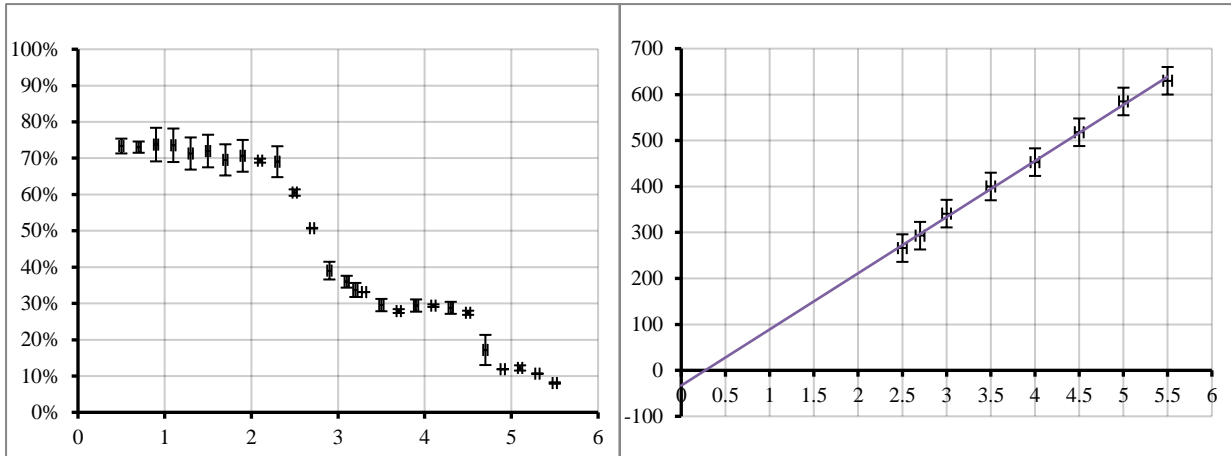


Figure 15 Bi sample percentage as a function of heating current (amps) before anneal. Figure 16 Temperature (degrees) as a function of heating current (amps) before anneal.

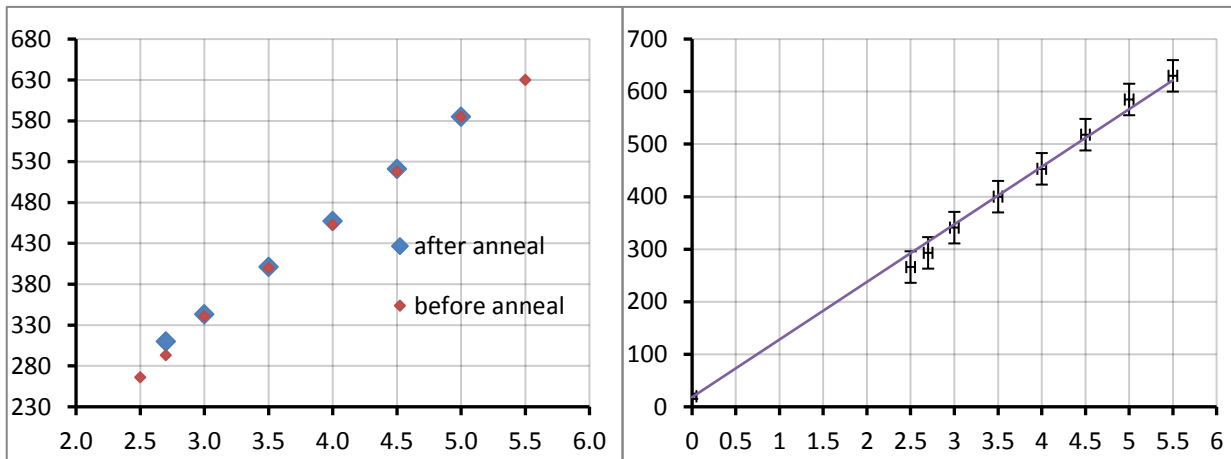


Figure 17 Temperature (degrees) as a function of heating current (amps) after sample anneal. Figure 18 Temperature (degrees) as a function of heating current (amps) before sample anneal.

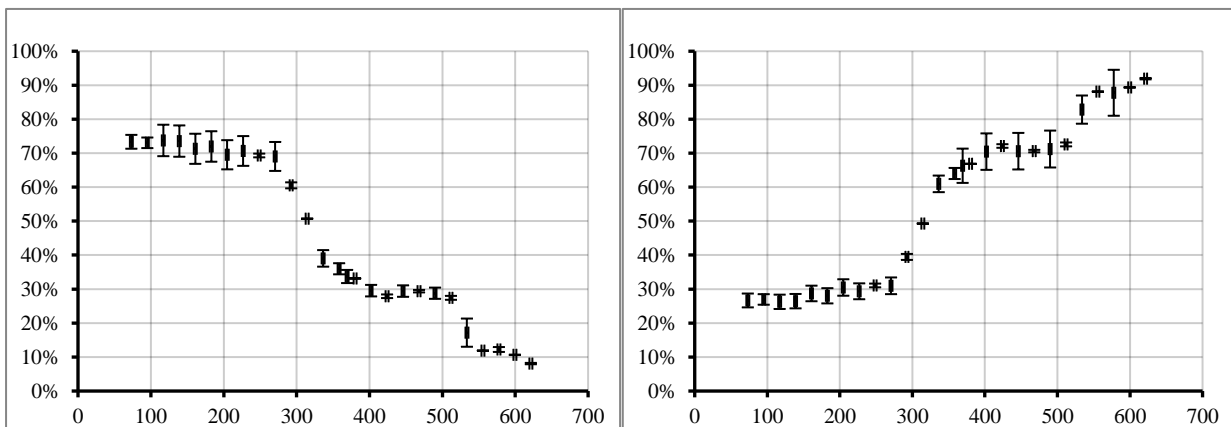


Figure 19 Bi sample percentage as a function of temperature (degrees). Figure 20 Al-Pd-Mn sample percentage as a function of temperature (degrees).

orbital	λ	$\delta\lambda$	K.E. (eV)	δ K.E. (eV)
Pd3d	13	6	1149	3
Al2s	8	6	1368	3
Al2p	13	20	1413	3
Mn 2p	9	8	848	3

Table 2. the IMFPs of Bi for a range of electron orbitals and electron energies.

The theoretical predictions of the IMFP's of various elements has been previously calculated by Tanuma et al²⁶. This work fits the calculated IMFPs to the Bethe equation for inelastic electron scattering in matter. The IMFP λ , is given by

$$\lambda = \frac{E}{E_p^2 \left(\beta \ln(\gamma E) - \frac{C}{E} + \frac{D}{E^2} \right)}$$

Where E is the photoelectron energy (eV),

$$\beta = -0.0216 + \frac{0.994}{(E_p^2 + E_g^2)^{1/2}} + 7.39 \times 10^{-4} \cdot \rho$$

Where E_p is the Plasmon energy and E_g is the band gap energy eV

$$\gamma = 0.191 \cdot \rho^{1/2}$$

$$C = 1.97 - 0.91 \cdot U$$

$$D = 53.4 - 20.8 \cdot U$$

$$U = \frac{N_v \rho}{M}$$

Where N_v is the number of valence electrons, ρ is the density ($\text{g}\cdot\text{cm}^{-3}$) and M is the atomic mass.

Figure 25 shows that the experimental values of the IMFPs are consistently lower than the values predicted by the Tanuma model. Recent research has indicated that this discrepancy could be due to surface excitations⁴². The theoretical IMFP plotted in figure 25 arise from considering bulk solids. It would be expected that modifications to the IMFPs should occur in the vicinity of surfaces, mainly due to surface Plasmon excitations.

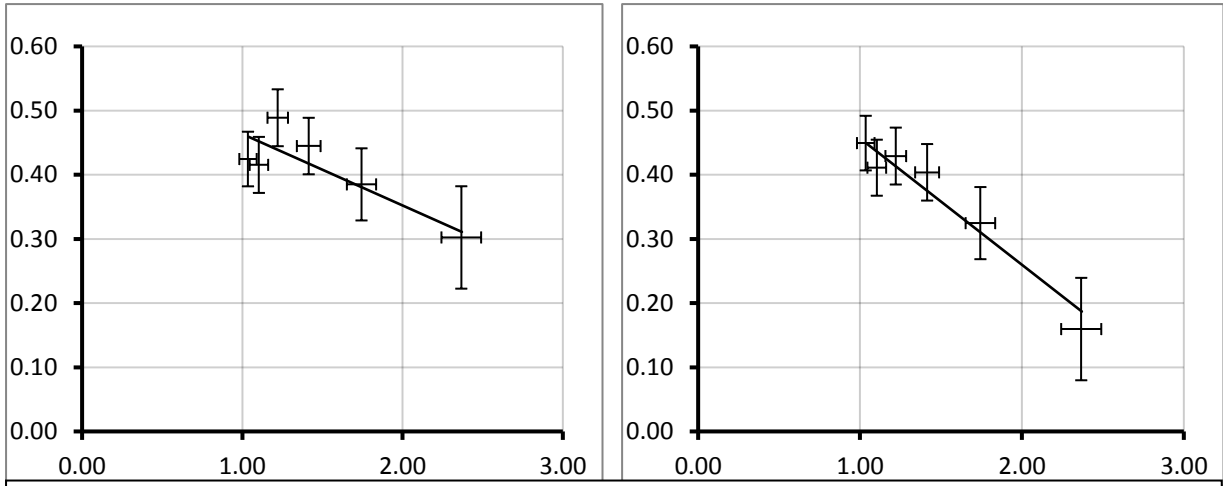


Figure 21 Ln clean Pd3d intensity minus ln of Bi monolayerPd3d intensity as a function of 1/cosθ. figure 22 Ln clean Al2s intensity minus ln of Bi monolayerAl2s intensity as a function of 1/cosθ.

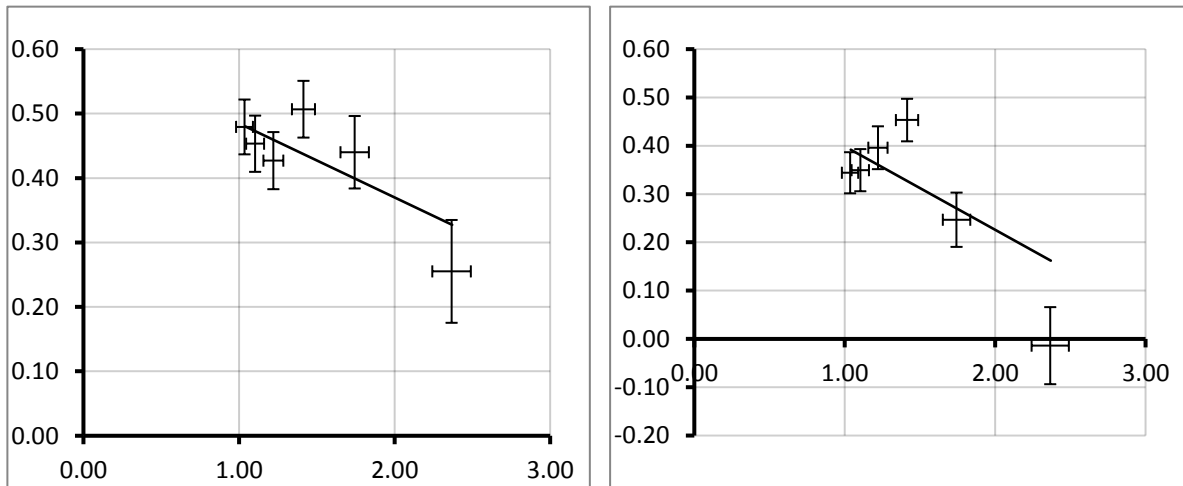


Figure 23 Ln clean Al2p intensity minus ln of Bi monolayerAl2p intensity as a function of 1/cosθ. figure 24 Ln clean Mn2p intensity minus ln of Bi monolayerMn2p intensity as a function of 1/cosθ.

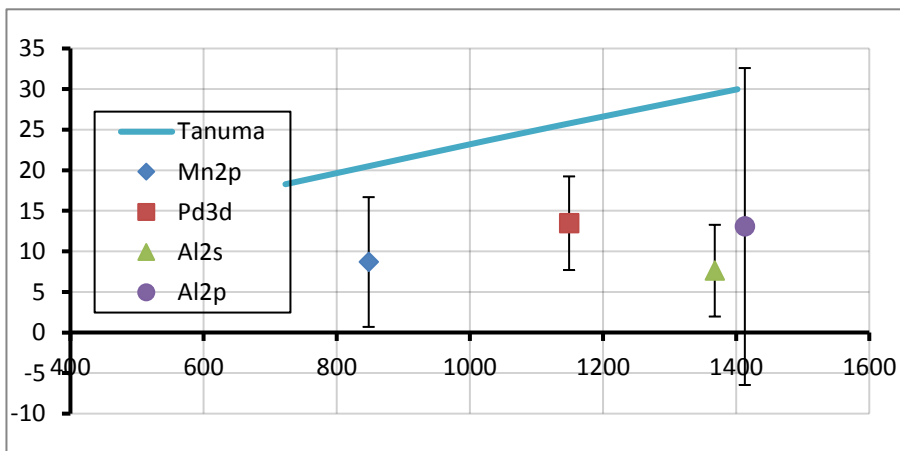


Figure 25 IMFP (Angstroms) as a function of energy (KeV)with Tanuma relationship

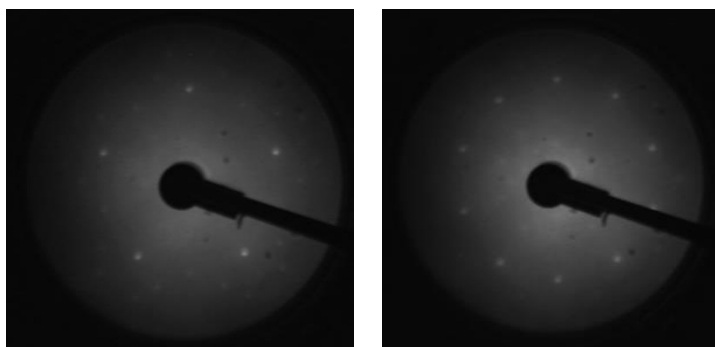


Figure 26. LEED pattern of Bi monolayer sample at 82 eV. Figure 27. LEED pattern of Bi monolayer sample at 64 eV

Figures 26 and 27 are LEED patterns of the sample with a monolayer of Bi, taken towards the end of the experiment. The five fold and ten fold symmetry of the Bi on Al-Pd-Mn system is clearly observed in figures 26 and 27 respectively. On completion of the spectroscopic experiment the sample was moved to the STM chamber to scan the Bi multilayer on Al-Pd-Mn. The STM images seemed to indicated that the multilayer grows with a pseudo-cubic growth.

Analysis

The time taken to deposit a monolayer of Bi onto a clean Al-Pd-Mn surface at 120nA Bi flux was (31 ± 3) Minutes (11% error). The Bi multilayer appears to desorb over the temperature range 275 – 400 degrees. The monolayer desorbs over the temperature range 500 - 625 degrees. The experimental values of the IMFPs of Bi are summarised in table 2.

Conclusion

In terms of providing complementary results to previous work this project appears to have achieved its goal. However, in part due to my inexperience on the apparatus and perhaps a fundamental misunderstanding of the project at large from the start, much if the intended experiment was not performed. It was expected that high resolution XPS data would be obtained to determine some asymmetry in peaks to provide evidence as to which element Bi was bonding to. The experiment would have been improved had there been time to obtain Ultra Violet Photoelectron Spectroscopy (UPS) which would have provided information on the valance electrons in the system. Somewhere in-between my willingness to let others perform the experiment and a complete lack of formal training on the expensive equipment laid the reason behind a barrage of mistakes that ultimate led the project to run haphazardly, uncoordinatedly and out of time. In the event of performing the experiment again a strict

and thoughtful day to day plan would be laid out for the project. Rather than rushing from one experimental set up to another, plenty of time would be allowed for quiet thought and reflection on the experiment. This methodical procedure would ensure that time lost in experimental planning would be less than the time saved by not making errors in the experimental procedure. In future one person should be in control of the experiment with advice and help from colleges available whenever it is required. With two experimenters sharing responsibility a war of ideas over which direction the experiment should go inevitably arises. Had the experiment been recorded in my laboratory book the left hand page would have been left only for the recording of experimental comments and observations. The right hand page would have been neat clear and concise, with the date, time and every other relevant statistic appearing above every recording. The conflict of initiatives led to two different naming systems for the XPS filenames which rendered the analytical process far more difficult than it needed to be.

The experiment was a huge learning curve and provided an excellent opportunity for me to apply the skills, knowledge and techniques I have learnt over the last four years of university. For running the experiment appreciation is extended to Kirsty Young. Dr. V. Dhanak, whose knowledge and experience in the field of matter physics was invaluable to the day to day running of the experiment, is thanked. Dr. H.R. Sharma is thanked for providing an exciting and un-researched topic of physics for me to base my masters project on and for help in discussing the project. Dr. J. Smerdon is thanked for his talented operation of the STM apparatus and continued advice throughout the experiment. J.K. Parle is thanked for help with the operation of the software programme casa XPS.

References

1. Smerdon JA, Parle JK, Wearing LH, Lograsso TA, Ross AR, McGrath R. Nucleation and growth of a quasicrystalline monolayer: Bi adsorption on the fivefold surface of i -Al₇₀Pd₂₁Mn₉. *Physical Review B - Condensed Matter and Materials Physics* 2008;78(7).
2. Sharma HR, Fournée V, Shimoda M, Ross AR, Lograsso TA, Gille P, Tsai AP. Growth of bi thin films on quasicrystal surfaces. *Physical Review B - Condensed Matter and Materials Physics* 2008;78(15).
3. Levine D, Steinhardt PJ. Quasicrystals: A new class of ordered structures. *Phys Rev Lett* 1984;53(26):2477-80.
4. Binnig G, Rohrer H, Gerber C, Weibel E. Surface studies by scanning tunneling microscopy. *Phys Rev Lett* 1982;49(1):57-61.
5. Janot C. *Quasicrystals A primer*. Second ed. Oxford: Clarendon Press; 1994. .

6. Dubois J-, Brunet P, Costin W, Merstallinger A. Friction and fretting on quasicrystals under vacuum. *J Non Cryst Solids* 2004;334-335:475-80.
7. Takeuchi S, Akiyama H, Naito N, Shibuya T, Hashimoto T, Edagawa K, Kimura K. Electrical resistivity of single-grained quasicrystals. *J Non Cryst Solids* 1993;153-154(C):353-6.
8. Ledieu J, Hoelt JT, Reid DE, Smerdon JA, Diehl RD, Lograsso TA, Ross AR, McGrath R. Pseudomorphic growth of a single element quasiperiodic ultrathin film on a quasicrystal substrate. *Phys Rev Lett* 2004;92(13):135507-1.
9. Franke KJ, Sharma HR, Theis W, Gille P, Ebert P, Rieder KH. Quasicrystalline epitaxial single element monolayers on icosahedral al-pd-mn and decagonal al-ni-co quasicrystal surfaces. *Phys Rev Lett* 2002;89(15):156104/1,156104/4.
10. Krajčí M, Hafner J. Ab-initio study of a quasiperiodic bi monolayer on a fivefold icosahedral al-pd-mn surface. *Philosophical Magazine* 2006;86(6-8):825-30.
11. Shen Z, Stoldt CR, Jenks CJ, Lograsso TA, Thiel PA. Fine structure on flat surfaces of quasicrystalline al-pd-mn. *Physical Review B - Condensed Matter and Materials Physics* 1999;60(21):14688-94.
12. Sharma HR. *Surface physics*. 2008.
13. Farnsworth HE, Schlier RE, George TH, Burger RM. Ion bombardment-cleaning of germanium and titanium as determined by low-energy electron diffraction [4]. *J Appl Phys* 1955;26(2):252-3.
14. Einstein A. *On a heuristic viewpoint concerning the production and transformation of light*. *Annalen Der Physik* 1905;1(1):1-.
15. Bouguer P. *Essai d'optique sur la gradation de la lumi re*. NA ed. France: NA; 1729. .
16. Kittel C. *Introduction to solid state physics*. 7th ed. Cambridge: Wiley; 1995. .
17. Yates K, Barrie A, Street FJ. A double-anode X-ray source for photoelectron spectroscopy. *Journal of Physics E: Scientific Instruments* 1973;6(2):130-2.
18. Prutton M. *Introduction to surface physics*. 1st ed. Great Britain: Oxford University Press; 1995. .
19. Briggs, D. Grant, G. T. *Surface analysis by auger and X-ray photoelectron spectroscopy*. First ed. Towbridge: The Cromwell Press; 2003. .
20. Fadley CS, Baird RJ, Siekhaus W, Novakov T, Bergstr m SAL. Surface analysis and angular distributions in x-ray photoelectron spectroscopy. *Journal of Electron Spectroscopy and Related Phenomena* 1974;4(2):93-137.
21. Penn DR. Quantitative chemical analysis by ESCA. *Journal of Electron Spectroscopy and Related Phenomena* 1976;9(1):29-40.
22. Jenkin JG, Riley JD, Liesegang J, Leckey RCG. The development of X-ray photoelectron spectroscopy (1900-1960): A postscript. *Journal of Electron Spectroscopy and Related Phenomena* 1978;14(6):477-85.

23. Purcell EM. The focusing of charged particles by a spherical condenser. *Physical Review* 1938;54(10):818-26.
24. Redhead PA. Measurement of vacuum; 1950-2003. *Journal of Vacuum Science and Technology A: Vacuum, Surfaces and Films* 2003;21(5):S1-6.
25. Dhanak V. *Spectroscopic discussions*. 2009.
26. Tanuma S, Powell CJ, Penn DR. Calculations of electron inelastic mean free paths. II. data for 27 elements over the 50-2000 eV range. *Surf Interface Anal* 1991;17(13):911-26.
27. Cahn JWS, D. *The physics of quasicrystals*. 2nd ed. France: Wiley; 1985. .
28. Quivy A, Quiquandon M, Calvayrac Y, Faudot F, Gratiat D, Berger C, Brand RA, Simonet V, Hippert F. A cubic approximant of the icosahedral phase in the (al-si)-cu-fe system. *Journal of Physics Condensed Matter* 1996;8(23):4223-34.
29. Razavy M. *Quantum theory of tunneling*. 1st ed. U.K.: World Scientific Publications; 2002. .
30. Eisberg RR, R. *Quantum physics of atoms, molecules, solids, nuclei and particles*. 2nd ed. America: John Wiley and Sons; 1985. .
31. Mandl F. *Quantum mechanics*. 1st ed. Manchester: WileyBlackwell; 1992. .
32. Parle JK. *Laboratory discussion*. 2009.
33. Briggs D. *Handbook of X-ray and photoelectron spectroscopy*. 1st ed. Nottingham: Heyden; 1977. .
34. Stranski INK, V. *Abhandlungen der mathematisch-naturwissenschaftlichen klasse*. . Akademie Der Wissenschaften Und Der Literatur in Mainz 1939;1(1):1-10.
35. Venables JA, Spiller GDT, Hanbucken M. Nucleation and growth of thin films. *Reports on Progress in Physics* 1984;47(4):399-459.
36. Nagl C, Platzgummer E, Schmid M, Varga P, Speller S, Heiland W. Subsurface islands and superstructures of cu on pb(111). *Surf Sci* 1996;352-354:540-5.
37. Pimpinelli A. *Physics of crystal growth*. 1st ed. United Kingdom: Cambridge University Press; 1999. .
38. Venables JA. *Introduction to thin film process*. 1st ed. United Kingdom: Cambridge university press; 2008. .
39. Smerdod JA. 2009.
40. Fairly N. *Casa XPS [computer program]*. United Kingdom: 1994. .
41. Hutchcroft D. *Java JLineFit [computer program]*. University of Liverpool: 1998. .
42. Jablonski A, Lesiak B, Zemek J, Jiricek P. Determination of the electron inelastic mean free path for samarium. *Surf Sci* 2005;595(1-3):1-5.

Appendix

Raw data and analytical data for 400nA Bi flux

Flux (nA)	δ	Time (mins)	δ	Time mins (flux= 120 A)	δ
400	10	1.5	0.17	5	0.56
400	10	3.75	0.17	13	0.56
400	10	7.5	0.17	25	0.56
400	10	11.25	0.17	38	0.56
400	10	11.25	0.17	38	0.56
400	10	15	0.17	50	0.56
400	10	18.75	0.17	63	0.56
400	10	20	0.17	67	0.56

emission angle (degrees)	Bi 4f7/2 intensity		δ	Bi Sensitivity	δ	Bi normed
0	1786	1786	200	9.14	0.0914	195
0	4068	4068	200	9.14	0.0914	445
0	7193	7193	200	9.14	0.0914	787
0	9313	9313	200	9.14	0.0914	1019
0	550	550	20	9.14	0.0914	60
0	8994	8994	200	9.14	0.0914	984
0	10505	10505	200	9.14	0.0914	1149
0	14179	14179	141	9.14	0.0914	1551

δ	Al 2p intensity		δ	Al sensitivity	δ	Al normed	δ
22	2737	2737	50	0.19	0.0019	14181.35	260.49
22	2582	2582	50	0.19	0.0019	13378.24	260.41
23	2085	2085	50	0.19	0.0019	10803.11	260.15
24	2302	2302	50	0.19	0.0019	11927.46	260.26
2	136	136	2	0.19	0.0019	704.66	10.43
24	2017	2017	50	0.19	0.0019	10450.78	260.11
25	1923	1923	50	0.19	0.0019	9963.73	260.06
22	212	2744	50	0.19	0.0019	14219.68	260.49

Pd 3d intensity		δ	Pd sensitivity	δ	Pd normed	δ	Mn 2p intensity
15854	15854	50	4.62	0.0462	3431.60	11.17	5624
14610	14610	50	4.62	0.0462	3162.34	11.14	4973
13375	13375	50	4.62	0.0462	2895.02	11.11	4703
13055	13055	50	4.62	0.0462	2825.76	11.11	4156
782	782	2	4.62	0.0462	169.26	0.45	162
11149	11149	50	4.62	0.0462	2413.20	11.06	2185
10473	10473	50	4.62	0.0462	2266.88	11.05	2176
1207	15625	50	4.62	0.0462	3382.02	11.16	3544

	δ	Mn sensitivity	δ	Mn normed	δ	sum of intensity	δ
3085	50	2.42	0.0242	1274.79	20.79	19083	261
2573	50	2.42	0.0242	1063.22	20.77	18049	261
2496	50	2.42	0.0242	1031.40	20.76	15517	261
2144	50	2.42	0.0242	885.95	20.75	16658	261
162	2	2.42	0.0242	66.94	0.83	1001	11
2185	50	2.42	0.0242	902.89	20.75	14751	261
2176	50	2.42	0.0242	899.17	20.75	14279	261
3620	50	2.42	0.0242	1495.87	20.81	20649	261

Bi normed	δ	Al normed	δ	Pd normed	δ	Mn normed	δ
1.0%	0.1%	74.3%	1.7%	18.0%	2.1%	6.7%	0.2%
2.5%	0.1%	74.1%	1.8%	17.5%	1.0%	5.9%	0.2%
5.1%	0.2%	69.6%	2.0%	18.7%	0.8%	6.6%	0.2%
6.1%	0.2%	71.6%	1.9%	17.0%	0.7%	5.3%	0.2%
6.0%	0.2%	70.4%	1.3%	16.9%	0.7%	6.7%	0.1%
6.7%	0.2%	70.8%	2.2%	16.4%	0.7%	6.1%	0.2%
8.0%	0.3%	69.8%	2.2%	15.9%	0.6%	6.3%	0.2%
7.5%	0.2%	68.9%	1.5%	16.4%	0.4%	7.2%	0.2%

AIPdMn	δ	AIPdMn normed	δ
18887.7423	261.55	99.0%	11.5%
17603.7991	261.47	97.5%	5.7%
14729.5354	261.21	94.9%	4.3%
15639.1691	261.32	93.9%	3.9%
940.8694	10.48	94.0%	4.1%
13766.8732	261.17	93.3%	4.1%
13129.7872	261.12	92.0%	4.0%
19097.5694	261.56	92.5%	2.6%

Linefits for 400nA Bi flux data

Bi submonolayer

	Value	Error
Gradient	0.006814815	6.E-04
Intercept	-3.25E-04	2.E-04
ChiSq/NDF	0.02	
	X	Y
Point 1	1.5	0.009897
Point 2	7.5	0.05

	X	Y
Point 1	1.5	0
Point 2	9	0.06

Bi multilayer

	Value	Error
Gradient	2.10E-03	5.17E-04
Intercept	0.036729307	0.0072181
ChiSq/NDF	0.45	
	X	Y
Point 1	11.25	0.06
Point 2	20	0.08

	X	Y
Point 1	6	0.05
Point 2	20	0.08

Al sub monolayer

	Value	Error
Gradient	-0.007964243	1.03E-02
Intercept	0.76	0.040293
ChiSq/NDF	0.12	
	X	Y
Point 1	1.5	0.75
Point 2	7.50	0.70

	X	Y
Point 1	1.5	1
Point 2	6	0.71

Al post monolayer

	Value	Error
Gradient	-1.72E-03	4.41E-03
Intercept	0.73	0.07763158
ChiSq/NDF	0.03	
	X	Y
Point 1	11.25	0.71
Point 2	20	0.69

	X	Y
Point 1	4	0.72
Point 2	20	0.69

AIPdMn sub monolayer

	Value	Error
Gradient	-0.0072	2.03E-03

AIPdMn post monolayer

	Value	Error
Gradient	-2.51E-03	7.44E-04

[Type text]

[Type text]

Nick Cross
200365040

Intercept	1.00	0.121938
ChiSq/NDF	0.00	
	X	Y
Point 1	1.5	0.99
Point 2	7.50	0.95

Intercept	0.97	0.136556
ChiSq/NDF	0.00	
	X	Y
Point 1	11.25	0.94
Point 2	20	0.92

	X	Y
Point 1	1.5	1
Point 2	10	0.93

	X	Y
Point 1	6	0.95
Point 2	20	0.92

	Value	Error
Gradient	0.002944	2.E-04
Intercept	-0.00589	3.E-03
ChiSq/NDF	1.41	
	X	Y
Point 1	5	0.008829
Point 2	25	0.07

	Value	Error
Gradient	-0.003	5.E-03
Intercept	1.006459	6.E-02
ChiSq/NDF	0.00	
	X	Y
Point 1	5	0.991448
Point 2	25	0.93

	Value	Error
Gradient	0.002933	2.E-04
Intercept	-0.00574	3.E-03
ChiSq/NDF	1.26	
	X	Y
Point 1	5	0.008928
Point 2	25	0.07

	Value	Error
Gradient	-0.003	5.E-03
Intercept	1.006459	6.E-02
ChiSq/NDF	0.00	
	X	Y
Point 1	5	0.991448
Point 2	25	0.93

Raw data and analytical data for 120nA + 400nA Bi flux data

Flux (nA)	δ	Time (mins)	δ	Time mins (flux= 120 A)	δ
120	10	8	0.03	8	0.67
120	10	12	0.03	12	1.00
120	10	16	0.03	16	1.33

[Type text]

[Type text]

Nick Cross
200365040

120	10	20	0.03	20	1.67
400	10	11.25	0.03	38	0.94
400	10	20	0.03	67	1.67
1000	10	10	0.03	83	0.88
1000	10	20	0.03	167	1.69
1000	10	30	0.03	250	2.52

emission angle (degrees)	Bi 4f7/2 intensity	FWHM	Bi Sensitivity	δ	Bi normed	δ
0	143.10	0.91	9.14	0.0914	15.66	0.19
0	202.00	1.10	9.14	0.0914	22.10	0.25
0	221.80	1.11	9.14	0.0914	24.27	0.27
0	287.30	1.06	9.14	0.0914	31.43	0.33
0	552.30	1.11	9.14	0.0914	60.43	0.62
0	862.60	1.15	9.14	0.0914	94.38	0.95
0	397.00	1.08	9.14	0.0914	43.44	0.45
0	495.50	1.07	9.14	0.0914	54.21	0.55
0	744.50	1.03	9.14	0.0914	81.46	0.82

Al 2p intensity	FWHM	Al sensitivity	δ	Al normed	δ	Al / Bi	δ
118.00	1.09	0.19	0.0019	611.40	8.31	0.82	0.01
120.70	1.10	0.19	0.0019	625.39	8.46	0.60	0.01
132.40	1.15	0.19	0.0019	686.01	9.09	0.60	0.01
110.60	1.05	0.19	0.0019	573.06	7.91	0.38	0.00
135.20	1.16	0.19	0.0019	700.52	9.24	0.24	0.00
208.50	1.44	0.19	0.0019	1080.31	13.14	0.24	0.00
85.90	0.93	0.19	0.0019	445.08	6.55	0.22	0.00
79.30	0.89	0.19	0.0019	410.88	6.18	0.16	0.00
88.20	0.94	0.19	0.0019	456.99	6.68	0.12	0.00

Mn 2p intensity	δ	Mn sensitivity	δ	Mn normed	δ	Pd 3d intensity
136.00	1.17	1.70	0.0170	80.00	1.05	744.00
134.00	1.16	1.70	0.0170	78.82	1.04	733.00
134.00	1.16	1.70	0.0170	78.82	1.04	832.00
132.00	1.15	1.70	0.0170	77.65	1.03	686.00
156.00	1.25	1.70	0.0170	91.76	1.18	782.00
251.00	1.58	1.70	0.0170	147.65	1.75	1209.00
107.00	1.03	1.70	0.0170	62.94	0.88	492.00
102.00	1.01	1.70	0.0170	60.00	0.84	485.00
102.00	1.01	1.70	0.0170	60.00	0.84	557.00

δ	Pd sensitivity	δ	Pd normed	δ	sum of intensity	δ	Bi normed	δ
2.73	2.70	0.0270	275.56	2.93	982.61	8.31	0.02	0.0003
2.71	2.70	0.0270	271.48	2.89	997.79	8.46	0.02	0.0004
2.88	2.70	0.0270	308.15	3.26	1097.25	9.09	0.02	0.0004
2.62	2.70	0.0270	254.07	2.72	936.21	7.91	0.03	0.0006
2.80	2.70	0.0270	289.63	3.08	1142.34	9.26	0.05	0.0009
3.48	2.70	0.0270	447.78	4.66	1770.11	13.18	0.05	0.0008
2.22	2.70	0.0270	182.22	2.00	733.68	6.56	0.06	0.0011
2.20	2.70	0.0270	179.63	1.97	704.72	6.20	0.08	0.0014
2.36	2.70	0.0270	206.30	2.24	804.75	6.73	0.10	0.0018

Al-Pd-Mn normed	δ	Al/Bi
0.98	0.01	61.76
0.98	0.01	44.15
0.98	0.01	44.22
0.97	0.01	28.78
0.95	0.01	17.90
0.95	0.01	17.76
0.94	0.01	15.89
0.92	0.01	12.00
0.90	0.01	8.88

Linefits for 120nA + 400nA Bi flux data

Bi submonolayer

	Value	Error
Gradient	0.00108	4.E-05
Intercept	0.0089	8.E-04
ChiSq/NDF	11.04	
	X	Y
Point 1	8	0.0175411
Point 2	38	0.05

	X	Y
Point 1	8	0
Point 2	37	0.05

Bi post monolayer

	Value	Error
Gradient	2.47E-04	4.83E-05
Intercept	0.037126	4.50E-03
ChiSq/NDF	0.56	
	X	Y
Point 1	38	0.05
Point 2	250	0.10

	X	Y
Point 1	25	0.04
Point 2	250	0.10

Al sub
monolayer

	Value	Error
Gradient	-1.09E-03	4.49E-04
Intercept	0.99	0.009279
ChiSq/NDF	0.13	
	X	Y
Point 1	8	0.98
Point 2	38.00	0.95

	X	Y
Point 1	8	0.98
Point 2	37	0.95

Al post
monolayer

	Value	Error
Gradient	-2.61E-04	6.98E-05
Intercept	0.96	0.010915
ChiSq/NDF	0.09	
	X	Y
Point 1	67	0.95
Point 2	250	0.90

	X	Y
Point 1	25	0.96
Point 2	250	0.90

Desorption raw data and analytical data

Bi 4F	δ	Bi4f sensitivity	Bi 4Fnormed	δ	Pd 3d	δ
24893	1245	9.140	2724	136	3844	192
24469	1223	9.140	2677	134	3566	178
24245	1212	9.140	2653	133	3424	171
23462	1173	9.140	2567	128	3581	179
28330	1417	9.140	3100	155	4249	212
28867	1443	9.140	3158	158	4350	218
26831	1342	9.140	2936	147	4353	218
27903	1395	9.140	3053	153	4396	220
27503	1375	9.140	3009	150	4538	227
27162	1358	9.140	2972	149	4158	208
27669	1383	9.140	3027	151	4197	210
26118	1306	9.140	2858	143	4693	235
26513	1326	9.140	2901	145	4395	220
24205	1210	9.140	2648	132	4492	225
30464	1523	9.140	3333	167	5729	286
25130	1257	9.140	2749	137	4863	243
25484	1274	9.140	2788	139	4821	241

26124	1306	9.140	2858	143	4492	225
19750	988	9.140	2161	108	4815	241
19100	955	9.140	2090	104	5145	257
19000	950	9.140	2079	104	5046	252
18600	930	9.140	2035	102	5343	267
19160	958	9.140	2096	105	5277	264
15050	753	9.140	1647	82	6450	323
15170	759	9.140	1660	83	6088	304
15270	764	9.140	1671	84	6182	309
11340	567	9.140	1241	62	7766	388
10340	517	9.140	1131	57	7634	382
9887	494	9.140	1082	54	8126	406
9573	479	9.140	1047	52	8439	422
9404	470	9.140	1029	51	7836	392
9157	458	9.140	1002	50	7936	397
8990	450	9.140	984	49	7866	393
8615	431	9.140	943	47	8091	405
8390	420	9.140	918	46	8241	412
8316	416	9.140	910	45	7866	393
6742	337	9.140	738	37	7491	375
6586	329	9.140	721	36	7142	357
6323	316	9.140	692	35	7099	355
6542	327	9.140	716	36	7581	379
6507	325	9.140	712	36	7316	366
6481	324	9.140	709	35	7513	376
6850	343	9.140	749	37	7660	383
6187	309	9.140	677	34	7218	361
6263	313	9.140	685	34	7773	389
6320	316	9.140	691	35	8016	401
5010	251	9.140	548	27	8863	443
4077	204	9.140	446	22	8825	441
3010	151	9.140	329	16	9614	481
2937	147	9.140	321	16	9253	463
2644	132	9.140	289	14	9841	492
2570	129	9.140	281	14	9474	474
2644	132	9.140	289	14	9547	477
2445	122	9.140	268	13	9778	489
2393	120	9.140	262	13	9318	466
1887	94	9.140	206	10	9110	456
1884	94	9.140	206	10	9423	471

Pd3d sensitivity	Pd3d normed	δ	Pd/Bi	δ	Mn	δ	Mn sensitivity
9.48	405	20	0.13	0.01	596.00	29.80	2.42

9.48	376	19	0.13	0.01	753.00	37.65	2.42
9.48	361	18	0.14	0.01	789.00	39.45	2.42
9.48	378	19	0.13	0.01	819.00	40.95	2.42
9.48	448	22	0.14	0.01	1069.00	53.45	2.42
9.48	459	23	0.16	0.01	861.50	43.08	2.42
9.48	459	23	0.15	0.01	1042.00	52.10	2.42
9.48	464	23	0.13	0.01	1028.00	51.40	2.42
9.48	479	24	0.15	0.01	1154.00	57.70	2.42
9.48	439	22	0.14	0.01	1217.00	60.85	2.42
9.48	443	22	0.14	0.01	939.00	46.95	2.42
9.48	495	25	0.16	0.01	970.00	48.50	2.42
9.48	464	23	0.17	0.01	1095.00	54.75	2.42
9.48	474	24	0.17	0.01	1027.00	51.35	2.42
9.48	604	30	0.17	0.01	1164.00	58.20	2.42
9.48	513	26	0.17	0.01	1067.00	53.35	2.42
9.48	509	25	0.17	0.01	1064.00	53.20	2.42
9.48	474	24	0.17	0.01	1339.00	66.95	2.42
9.48	508	25	0.24	0.01	1533.00	76.65	2.42
9.48	543	27	0.27	0.01	1435.00	71.75	2.42
9.48	532	27	0.27	0.01	1479.00	73.95	2.42
9.48	564	28	0.29	0.02	1131.00	56.55	2.42
9.48	557	28	0.28	0.01	1233.00	61.65	2.42
9.48	680	34	0.43	0.02	1306.00	65.30	2.42
9.48	642	32	0.40	0.02	1488.00	74.40	2.42
9.48	652	33	0.40	0.02	1166.00	58.30	2.42
9.48	819	41	0.68	0.04	1505.00	75.25	2.42
9.48	805	40	0.74	0.04	1269.00	63.45	2.42
9.48	857	43	0.82	0.04	1241.00	62.05	2.42
9.48	890	45	0.88	0.05	1265.00	63.25	2.42
9.48	827	41	0.83	0.04	1116.00	55.80	2.42
9.48	837	42	0.87	0.05	1157.00	57.85	2.42
9.48	830	41	0.87	0.05	1314.00	65.70	2.42
9.48	853	43	0.94	0.05	1530.00	76.50	2.42
9.48	869	43	0.98	0.05	1266.00	63.30	2.42
9.48	830	41	0.95	0.05	1268.00	63.40	2.42
9.48	790	40	1.11	0.06	1384.00	69.20	2.42
9.48	753	38	1.08	0.06	1432.00	71.60	2.42
9.48	749	37	1.12	0.06	1216.00	60.80	2.42
9.48	800	40	1.16	0.06	1300.00	65.00	2.42
9.48	772	39	1.12	0.06	1281.00	64.05	2.42
9.48	793	40	1.16	0.06	1230.00	61.50	2.42
9.48	808	40	1.12	0.06	1136.00	56.80	2.42
9.48	761	38	1.17	0.06	1121.00	56.05	2.42
9.48	820	41	1.24	0.07	1306.00	65.30	2.42
9.48	846	42	1.27	0.07	1488.00	74.40	2.42

[Type text]

[Type text]

Nick Cross
200365040

9.48	935	47	1.77	0.09	1166.00	58.30	2.42
9.48	931	47	2.16	0.11	1505.00	75.25	2.42
9.48	1014	51	3.19	0.17	1269.00	63.45	2.42
9.48	976	49	3.15	0.17	1241.00	62.05	2.42
9.48	1038	52	3.72	0.20	1265.00	63.25	2.42
9.48	999	50	3.69	0.19	1343.00	67.15	2.42
9.48	1007	50	3.61	0.19	1530.00	76.50	2.42
9.48	1031	52	4.00	0.21	1320.00	66.00	2.42
9.48	983	49	3.89	0.20	1632.00	81.60	2.42
9.48	961	48	4.83	0.25	1686.00	84.30	2.42
9.48	994	50	5.00	0.26	1793.00	89.65	2.42

Mn normed	δ	Al	δ	Al sensitivity	Al normed	δ	sum
246.28	12.31	895.00	44.75	0.19	4710.53	235.53	33694
311.16	15.56	753.00	37.65	0.19	3963.16	198.16	32309
326.03	16.30	997.00	49.85	0.19	5247.37	262.37	33242
338.43	16.92	1091.00	54.55	0.19	5742.11	287.11	33124
441.74	22.09	1170.00	58.50	0.19	6157.89	307.89	39179
355.99	17.80	879.70	43.99	0.19	4630.00	231.50	38203
430.58	21.53	1089.00	54.45	0.19	5731.58	286.58	37346
424.79	21.24	993.00	49.65	0.19	5226.32	261.32	37950
476.86	23.84	1080.00	54.00	0.19	5684.21	284.21	38202
502.89	25.14	952.00	47.60	0.19	5010.53	250.53	36833
388.02	19.40	1019.00	50.95	0.19	5363.16	268.16	37617
400.83	20.04	1031.00	51.55	0.19	5426.32	271.32	36638
452.48	22.62	1041.00	52.05	0.19	5478.95	273.95	36839
424.38	21.22	1081.00	54.05	0.19	5689.47	284.47	34811
480.99	24.05	1225.00	61.25	0.19	6447.37	322.37	43121
440.91	22.05	1067.00	53.35	0.19	5615.79	280.79	36050
439.67	21.98	1183.00	59.15	0.19	6226.32	311.32	36971
553.31	27.67	1268.00	63.40	0.19	6673.68	333.68	37843
633.47	31.67	1350.00	67.50	0.19	7105.26	355.26	32304
592.98	29.65	1384.00	69.20	0.19	7284.21	364.21	32122
611.16	30.56	1361.00	68.05	0.19	7163.16	358.16	31820
467.36	23.37	1118.00	55.90	0.19	5884.21	294.21	30295
509.50	25.48	1232.00	61.60	0.19	6484.21	324.21	31431
539.67	26.98	1445.00	72.25	0.19	7605.26	380.26	29645
614.88	30.74	1538.00	76.90	0.19	8094.74	404.74	29968
481.82	24.09	1548.00	77.40	0.19	8147.37	407.37	30081
621.90	31.10	1538.00	76.90	0.19	8094.74	404.74	27823
524.38	26.22	1751.00	87.55	0.19	9215.79	460.79	27714
512.81	25.64	1533.00	76.65	0.19	8068.42	403.42	26594
522.73	26.14	1760.00	88.00	0.19	9263.16	463.16	27798

[Type text]

[Type text]

Nick Cross
200365040

461.16	23.06	1311.00	65.55	0.19	6900.00	345.00	24601
478.10	23.90	1645.00	82.25	0.19	8657.89	432.89	26229
542.98	27.15	1555.00	77.75	0.19	8184.21	409.21	25583
632.23	31.61	1562.00	78.10	0.19	8221.05	411.05	25559
523.14	26.16	1551.00	77.55	0.19	8163.16	408.16	25317
523.97	26.20	1595.00	79.75	0.19	8394.74	419.74	25101
571.90	28.60	1523.00	76.15	0.19	8015.79	400.79	22821
591.74	29.59	1680.00	84.00	0.19	8842.11	442.11	23162
502.48	25.12	1743.00	87.15	0.19	9173.68	458.68	23098
537.19	26.86	1675.00	83.75	0.19	8815.79	440.79	23476
529.34	26.47	1476.00	73.80	0.19	7768.42	388.42	22121
508.26	25.41	1510.00	75.50	0.19	7947.37	397.37	22450
469.42	23.47	1583.00	79.15	0.19	8331.58	416.58	23311
463.22	23.16	1449.00	72.45	0.19	7626.32	381.32	21495
539.67	26.98	1445.00	72.25	0.19	7605.26	380.26	22181
614.88	30.74	1538.00	76.90	0.19	8094.74	404.74	23046
481.82	24.09	1549.00	77.45	0.19	8152.63	407.63	22507
621.90	31.10	1538.00	76.90	0.19	8094.74	404.74	21619
524.38	26.22	1751.00	87.55	0.19	9215.79	460.79	22364
512.81	25.64	1533.00	76.65	0.19	8068.42	403.42	20771
522.73	26.14	1760.00	88.00	0.19	9263.16	463.16	22271
554.96	27.75	1712.00	85.60	0.19	9010.53	450.53	21609
632.23	31.61	1672.00	83.60	0.19	8800.00	440.00	21623
545.45	27.27	1917.00	95.85	0.19	10089.47	504.47	22858
674.38	33.72	1932.00	96.60	0.19	10168.42	508.42	22554
696.69	34.83	2140.00	107.00	0.19	11263.16	563.16	22957
740.91	37.05	2222.00	111.10	0.19	11694.74	584.74	23743

δ	Bi norm	δ	Al-Pd-Mn norm	δ	Current (amps)	δ
1281	0.74	0.05	0.26	0.02	0.5	0.025
1252	0.76	0.05	0.24	0.02	0.5	0.025
1252	0.73	0.05	0.27	0.02	0.5	0.025
1221	0.71	0.04	0.29	0.02	0.5	0.025
1465	0.72	0.05	0.28	0.02	0.7	0.025
1478	0.76	0.05	0.24	0.02	0.7	0.025
1389	0.72	0.04	0.28	0.02	0.7	0.025
1436	0.74	0.05	0.26	0.02	0.7	0.025
1423	0.72	0.04	0.28	0.02	0.7	0.025
1397	0.74	0.05	0.26	0.02	0.9	0.025
1425	0.74	0.05	0.26	0.02	1.1	0.025
1354	0.71	0.04	0.29	0.02	1.3	0.025
1372	0.72	0.04	0.28	0.02	1.5	0.025
1264	0.70	0.04	0.30	0.02	1.7	0.025

1583	0.71	0.04	0.29	0.02	1.9	0.025
1310	0.70	0.04	0.30	0.02	2.1	0.025
1334	0.69	0.04	0.31	0.02	2.1	0.025
1367	0.69	0.04	0.31	0.02	2.3	0.025
1077	0.61	0.04	0.39	0.03	2.5	0.025
1054	0.59	0.04	0.41	0.03	2.5	0.025
1047	0.60	0.04	0.40	0.03	2.5	0.025
1012	0.61	0.04	0.39	0.03	2.5	0.025
1046	0.61	0.04	0.39	0.03	2.5	0.025
903	0.51	0.03	0.49	0.04	2.7	0.025
913	0.51	0.03	0.49	0.04	2.7	0.025
919	0.51	0.03	0.49	0.04	2.7	0.025
798	0.41	0.02	0.59	0.05	2.9	0.025
791	0.37	0.02	0.63	0.05	2.9	0.025
757	0.37	0.02	0.63	0.05	3.1	0.025
789	0.34	0.02	0.66	0.05	3.1	0.025
703	0.38	0.02	0.62	0.05	3.1	0.025
745	0.35	0.02	0.65	0.05	3.1	0.025
725	0.35	0.02	0.65	0.05	3.1	0.025
721	0.34	0.02	0.66	0.05	3.2	0.025
716	0.33	0.02	0.67	0.05	3.3	0.025
710	0.33	0.02	0.67	0.05	3.3	0.025
644	0.30	0.02	0.70	0.05	3.5	0.025
657	0.28	0.02	0.72	0.05	3.7	0.025
661	0.27	0.02	0.73	0.06	3.7	0.025
668	0.28	0.02	0.72	0.05	3.7	0.025
625	0.29	0.02	0.71	0.05	3.9	0.025
636	0.29	0.02	0.71	0.05	4.1	0.025
662	0.29	0.02	0.71	0.05	4.1	0.025
610	0.29	0.02	0.71	0.05	4.3	0.025
628	0.28	0.02	0.72	0.05	4.5	0.025
652	0.27	0.02	0.73	0.06	4.5	0.025
653	0.22	0.01	0.78	0.06	4.7	0.025
633	0.19	0.01	0.81	0.06	4.7	0.025
683	0.13	0.01	0.87	0.07	4.7	0.025
632	0.14	0.01	0.86	0.07	4.7	0.025
689	0.12	0.01	0.88	0.07	4.9	0.025
667	0.12	0.01	0.88	0.07	4.9	0.025
663	0.12	0.01	0.88	0.07	5.1	0.025
714	0.11	0.01	0.89	0.07	5.3	0.025
701	0.11	0.01	0.89	0.07	5.3	0.025
731	0.08	0.00	0.92	0.07	5.5	0.025
758	0.08	0.00	0.92	0.07	5.5	0.025

average		average		Time (mins)	δ	Temperature	δ
Bi norm	δ	Al-Pd- Mn norm	δ				
				10	0.17	73	2.03
				10	0.17	73	2.03
				10	0.17	73	2.03
0.733	0.020393335	0.27	0.020393	10	0.17	73	2.03
				10	0.17	95	2.03
				10	0.17	95	2.03
				10	0.17	95	2.03
				10	0.17	95	2.03
0.730	0.015536458	0.27	0.015536	10	0.17	95	2.03
0.737	0.05	0.26	0.02	10	0.17	117	2.03
0.736	0.05	0.26	0.02	10	0.17	139	2.03
0.713	0.04	0.29	0.02	10	0.17	161	2.03
0.720	0.04	0.28	0.02	10	0.17	183	2.03
0.695	0.04	0.30	0.02	11	0.17	205	2.03
0.706	0.04	0.29	0.02	12	0.17	227	2.03
				13	0.17	249	2.03
0.693	0.005512544	0.31	0.005513	14	0.17	249	2.03
0.690	0.04	0.31	0.02	10	0.17	271	2.03
				10	0.17	293	2.03
				10	0.17	293	2.03
				10	0.17	293	2.03
0.605	0.00883516	0.39	0.008835	10	0.17	293	2.03
				10	0.17	314	2.03
				10	0.17	314	2.03
0.507	0.00083037	0.49	0.00083	10	0.17	314	2.03
				10	0.17	336	2.03
0.390	0.024386294	0.61	0.024386	10	0.17	336	2.03
				10	0.17	358	2.03
				10	0.17	358	2.03
				10	0.17	358	2.03
				10	0.17	358	2.03
0.360	0.016356692	0.64	0.016357	10	0.17	358	2.03
0.337	0.02	0.66	0.05	10	0.17	369	2.03
				10	0.17	380	2.03
0.331	6.25914E-05	0.67	6.26E-05	10	0.17	380	2.03
0.295	0.02	0.70	0.05	10	0.17	402	2.03
				10	0.17	424	2.03
				10	0.17	424	2.03
0.279	0.005305639	0.72	0.005306	10	0.17	424	2.03
0.294	0.02	0.71	0.05	10	0.17	446	2.03

[Type text]

[Type text]

Nick Cross
200365040

				10	0.17	468	2.03
0.294	0.00365008	0.71	0.00365	10	0.17	468	2.03
0.288	0.02	0.71	0.05	10	0.17	490	2.03
				10	0.17	512	2.03
0.274	0.005742334	0.73	0.005742	10	0.17	512	2.03
				10	0.17	534	2.03
				10	0.17	534	2.03
				10	0.17	534	2.03
0.172	0.041515511	0.83	0.041516	10	0.17	534	2.03
				10	0.17	556	2.03
0.119	0.000147951	0.88	0.000148	10	0.17	556	2.03
0.122	0.01	0.88	0.07	10	0.17	578	2.03
				10	0.17	600	2.03
0.107	0.000610393	0.89	0.00061	0	0.17	600	2.03
				10	0.17	621	2.03
0.081	0.002012988	0.92	0.002013	10	0.17	621	2.03

Temperature calibration raw data

current	δ	temperature	δ	time	δ	temperature	δ
0.0	0.05	20	5	0	0.08	20	5
2.5	0.05	260	5	0	0.08	266	30
2.7	0.05	263	5	0	0.08	293	30
3.0	0.05	269	5	0	0.08	341	30
3.5	0.05	291	5	0	0.08	400	30
4.0	0.05	312	5	0	0.08	453	30
4.5	0.05	342	5	0	0.08	518	30
5.0	0.05	363	5	0	0.08	585	30
5.5	0.05	538	5	0	0.08	630	30

Temperature calibration linefit

	Value	Error
Gradient	109.6594	3.255279
Intercept	18.37117	7.33403
ChiSq/NDF	0.263533	
	X	Y

[Type text]

[Type text]

Nick Cross
200365040

Point 1	0	18.37117
Point 2	5.5	621.4978

	X	Y
point 0	0	18.37117
point 2	5.5	621.4978

IMFP Pd3d raw data and analytical data

I_0	δI_0	I	$d\delta I$	$\ln I_0$	δ	$\ln I$	δ	$\ln I_0 - \ln I$
13775	500	9010	200	9.53	0.04	9.11	0.02	0.42
13393	500	8841	200	9.50	0.04	9.09	0.02	0.42
13464	500	8258	200	9.51	0.04	9.02	0.02	0.49
13384	500	8579	200	9.50	0.04	9.06	0.02	0.44
10318	500	7021	200	9.24	0.05	8.86	0.03	0.38
7141	400	5278	300	8.87	0.06	8.57	0.06	0.30
3247	400	2084	300	8.09	0.12	7.64	0.14	0.44

δ	θ (degrees)	$\delta\theta$	θ (radians)	$\delta\theta$ (radians)	$\cos(\theta)$	$\delta \cos(\theta)$
0.04	15	3	0.26	0.052	0.97	0.051
0.04	25	3	0.44	0.052	0.91	0.047
0.04	35	3	0.61	0.052	0.82	0.043
0.04	45	3	0.79	0.052	0.71	0.037
0.06	55	3	0.96	0.052	0.57	0.030
0.08	65	3	1.13	0.052	0.42	0.022
0.19	75	3	1.31	0.052	0.26	0.014

$1/\cos\theta$	δ $1/\cos\theta$
1.04	0.05
1.10	0.06
1.22	0.06
1.41	0.07
1.74	0.09
2.37	0.12
3.86	0.20

IMFP Pd3d linefit

	Value	Error
Gradient	-0.11	0.05
Intercept	0.57	0.07
ChiSq/NDF	0.48	
	X	Y
Point 1	1.04	0.46
Point 2	2.37	0.31

IMFP Al2s raw data and analytical data

I_0	δI_0	I	δI	$\ln I_0$	δ	$\ln I$	δ	$\ln I_0 - \ln I$
3017	200	1925	100	8.01	0.07	7.56	0.05	0.45
3003	200	1991	150	8.01	0.07	7.60	0.08	0.41
2906	200	1892	200	7.97	0.07	7.55	0.11	0.43
3013	200	2012	200	8.01	0.07	7.61	0.10	0.40
2500	200	1807	200	7.82	0.08	7.50	0.11	0.32
1614	200	1376	200	7.39	0.12	7.23	0.15	0.16
799	200	714	200	6.68	0.25	6.57	0.28	0.11

δ	θ (degrees)	$\delta\theta$	θ (radians)	$\delta\theta$ (radians)	$\cos(\theta)$	$\delta \cos(\theta)$
0.08	15	3	0.26	0.052	0.97	0.051
0.10	25	3	0.44	0.052	0.91	0.047
0.13	35	3	0.61	0.052	0.82	0.043
0.12	45	3	0.79	0.052	0.71	0.037
0.14	55	3	0.96	0.052	0.57	0.030
0.19	65	3	1.13	0.052	0.42	0.022
0.38	75	3	1.31	0.052	0.26	0.014

$1/\cos\theta$	δ $1/\cos\theta$
1.04	0.05
1.10	0.06
1.22	0.06
1.41	0.07

[Type text]

[Type text]

Nick Cross
200365040

1.74	0.09
2.37	0.12
3.86	0.20

Al2s IMFP linefit

	Value	Error
Gradient	-0.20	0.15
Intercept	0.65	0.18
ChiSq/NDF	0.04	
	X	Y
Point 1	1.04	0.45
Point 2	2.37	0.19

IMFP Al2p raw data and analytical data

I_0	δI_0	I	δI	$\ln I_0$	δ	$\ln I$	δ	$\ln I_0 - \ln I$
2487	100	1540	100	7.82	0.040	7.34	0.065	0.48
2305	150	1465	150	7.74	0.065	7.29	0.10	0.45
2253	200	1470	200	7.72	0.089	7.29	0.14	0.43
2392	200	1441	200	7.78	0.084	7.27	0.14	0.51
1899	200	1223	200	7.55	0.105	7.11	0.16	0.44
1319	200	1022	200	7.18	0.1516	6.93	0.20	0.26
665	200	489	200	6.50	0.301	6.19	0.41	0.31

δ	θ (degrees)	$\delta\theta$	θ (radians)	$\delta\theta$ (radians)	$\cos(\theta)$	$\delta \cos(\theta)$
0.08	15	3	0.26	0.052	0.97	0.051
0.12	25	3	0.44	0.052	0.91	0.047
0.16	35	3	0.61	0.052	0.82	0.043
0.16	45	3	0.79	0.052	0.71	0.037
0.19	55	3	0.96	0.052	0.57	0.030
0.25	65	3	1.13	0.052	0.42	0.022
0.51	75	3	1.31	0.052	0.26	0.014

[Type text]

[Type text]

Nick Cross
200365040

$1/\cos\theta$	δ $1/\cos\theta$
1.04	0.05
1.10	0.06
1.22	0.06
1.41	0.07
1.74	0.09
2.37	0.12
3.86	0.20

AI2p IMFP linefit

	Value	Error
Gradient	-0.11	0.17
Intercept	0.60	0.21
ChiSq/NDF	0.10	
	X	Y
Point 1	1.04	0.48
Point 2	2.37	0.33

IMFP Mn2p raw data and analytical data

I_0	δI_0	I	δI	$\ln I_0$	δ	$\ln I$	δ	$\ln I_0 - \ln I$
3061	200	2170	100	8.03	0.065	7.68	0.05	0.34
2845	200	2006	150	7.95	0.070	7.60	0.07	0.35
2903	200	1954	150	7.97	0.069	7.58	0.08	0.40
2953	200	1877	150	7.99	0.068	7.54	0.08	0.45
2067	200	1615	200	7.63	0.097	7.39	0.12	0.25
1141	200	1157	200	7.04	0.175	7.05	0.17	-0.01
572	200	504	200	6.35	0.350	6.22	0.40	0.13

δ	θ (degrees)	$\delta\theta$	θ (radians)	$\delta\theta$ (radians)	$\cos(\theta)$	$\delta \cos(\theta)$
0.08	15	3	0.26	0.052	0.97	0.051
0.10	25	3	0.44	0.052	0.91	0.047
0.10	35	3	0.61	0.052	0.82	0.043
0.10	45	3	0.79	0.052	0.71	0.037
0.16	55	3	0.96	0.052	0.57	0.030

[Type text]

[Type text]

Nick Cross
200365040

0.25	65	3	1.13	0.052	0.42	0.022
0.53	75	3	1.31	0.052	0.26	0.014

$1/\cos\theta$	δ $1/\cos\theta$
1.04	0.05
1.10	0.06
1.22	0.06
1.41	0.07
1.74	0.09
2.37	0.12
3.86	0.20

Mn2p IMFP linefit

	Value	Error
Gradient	-0.17	0.16
Intercept	0.57	0.20
ChiSq/NDF	0.62	
	X	Y
Point 1	1.04	0.39
Point 2	2.37	0.16